chemosensors

MDPI

Article

MoS_2/Graphene Heterostructures as Gas Sensors for CO, CO_2, NO and HF

Abderrahim Bayou [1], Ahmed Kotbi [1], El Mehdi Nouizi [1,2], Bouchra Asbani [1], Abdelkrim Batan [2], Maryam AlQaydi [3], Ahmed Al-Shami [4], Bouchaib Hartiti [2] and Mustapha Jouiad [1,*]

[1] Laboratory of Physics of Condensed Matter, University of Picardie Jules Verne, Scientific Pole, 33 Rue Saint-Leu, CEDEX 1, 80039 Amiens, France; bouchra.asbani@u-picardie.fr (B.A.)
[2] Laboratoire de Mathématiques et Sciences Physiques Appliqués aux Sciences de L'Ingénieur, Hassan II University of Casablanca, FSTM BP, 146, Mohammedia 20650, Morocco
[3] Direct Energy Center, Technology Innovation Institute, Abu Dhabi P.O. Box 9639, United Arab Emirates
[4] Instituto de Ciencias Físicas, Universidad Nacional Autónoma de México, Cuernavaca 62210, Mexico
* Correspondence: mustapha.jouiad@u-picardie.fr

Abstract

The strategic integration of the tunable band gap and high carrier mobility of MoS_2 with the exceptional electrical conductivity of graphene offers a compelling route to circumvent the intrinsic sensing limitations of each material in isolation. Within the resulting van der Waals heterostructures, synergistic interlayer electronic coupling substantially reshapes the optoelectronic response. In particular, the MoS_2/graphene interface exhibits an ultraviolet absorption coefficient of approximately 3.5 × 105 cm^{-1} at 350 nm, an enhancement of about 20% relative to pristine MoS_2. First-principles density functional theory (DFT) calculations further show that tuning the interlayer spacing induces a finite band gap in graphene, attaining 67.8 meV at a compressed separation of 2.3 Å. Building on these electronic insights, the gas-sensing performance of the MoS_2/graphene heterostructure was evaluated toward CO, CO_2, NO, and HF gases. The adsorption energies, supported by electronegativity analysis, were consistently negative for oxidizing (CO_2, NO), reducing (CO), and corrosive (HF) molecules, namely −70 meV, −51 meV, −363 meV, and −127 meV for CO, CO_2, NO, and HF, respectively, a trend corroborated by electronegativity analysis. This energetically favorable adsorption underscores the strong gas–surface interactions enabled by the heterointerface, revealing a superior sensing response compared to either MoS_2 or graphene alone. These results highlight the promising potential of MoS_2/graphene heterostructures for next-generation, high-sensitivity gas-monitoring technologies.

Keywords: MoS_2/graphene; heterostructures; DFT calculations; optical properties; gas sensing

Check for updates

Received: 1 October 2026
Revised: 6 November 2026
Accepted: 10 November 2026
Published: 13 November 2026

Copyright: © 2026 by the authors. Licensee MDPI, Basel, Switzerland. This article is an open access article distributed under the terms and conditions of the Creative Commons Attribution (CC BY) license.

1. Introduction

Graphene, one of the most influential scientific discoveries of the twenty-first century, is a single atomic layer of sp^2-hybridized carbon atoms arranged in a hexagonal lattice and stabilized by sp^2 hybridization. Since its isolation [1], its exceptional physicochemical properties have attracted intense research interest. These include an ultrahigh theoretical specific surface area (~2630 $m^2 \cdot g^{-1}$) [2,3], outstanding mechanical strength [4–8], high optical transparency from the visible to the infrared [9], and exceptionally high carrier mobility (~200,000 $cm^2 \cdot V^{-1} \cdot s^{-1}$) [10–13]. Despite these advantages, the absence of an intrinsic band gap hinders the integration of graphene into electronic and photonic

devices. This challenge has motivated the exploration of alternative two-dimensional (2D) semiconductors and the engineering of van der Waals heterostructures that combine graphene with other layered materials offering controllable electronic structure. Among these, molybdenum disulfide (MoS_2) and related transition metal dichalcogenides (TMDs) have emerged as highly promising candidates [14–18]. TMDs possess a graphite-like layered structure described by the formula MX_2, where M is a transition metal (e.g., Mo, W) and X is a chalcogen (e.g., S, Se). Their intrinsic anisotropy leads to unique electrical, thermal, mechanical, and chemical characteristics. MoS_2 is the most widely studied TMD [19], existing in three major polymorphs: 1T (tetragonal), 2H (hexagonal), and 3R (rhombohedral) [20–22]. The 2H phase is the most thermodynamically stable, and consists of a molybdenum layer sandwiched between two sulfur planes through strong covalent Mo-S bonds. With a layer-dependent band gap tunable from 1.2 to 1.9 eV, MoS_2 offers a versatile platform for optoelectronic and sensing technologies [23,24]. It further provides excellent chemical stability and notable carrier mobility [25,26]. Consequently, MoS_2 has been deployed across diverse domains, including solid lubricants [27,28], gas sensors [29–31], DNA biosensors [32,33], lithium-ion batteries [34,35], photodetectors [36–38], photocatalysis [39–41], electrocatalysis [42], solar cells [43] light emitting diodes [44] and supercapacitors [45]. While bulk MoS_2 exhibits an indirect band gap of ~1.2 eV, its few-layer form transitions to a direct band gap of 1.8–1.9 eV [46–48], a nanoscale transformation that unlocks strong optical absorption and emission, making it a compelling alternative to gapless graphene for next-generation optoelectronics [49], and offering a way around graphene's zero-gap constraint [50]. These structural and electronic features enable the formation of stable monolayers with narrow yet tunable band gaps [51]. However, the modest carrier mobility of MoS_2 (~0.1–100 $cm^2 \cdot V^{-1} \cdot s^{-1}$) [52,53] limits its use in high-speed devices. To combine graphene's exceptional electronic transport with the semiconducting functionality of MoS_2, hybrid MoS_2/graphene heterostructures have attracted significant attention [54]. Advances in synthesis have enabled solution-processed graphene/MoS_2 networks prepared using L-cysteine, yielding three-dimensional architectures with excellent electrochemical performance for lithium-ion batteries [55]. Other notable examples include MoS_2 nanoparticle-decorated reduced graphene oxide with enhanced electrocatalytic activity for hydrogen evolution [56], graphene/MoS_2 nanofiber-based gas sensors [57], Schottky diodes grown by chemical vapor deposition [58], and high-performance field-effect transistors [59]. In parallel, recent experimental work has demonstrated the potential of heterojunction materials for gas-sensing applications [60]. Collectively, these reports highlight the transformative potential of MoS_2/graphene interfaces across electrochemical, electronic, and sensing technologies.

In this study, we employ first-principles DFT to analyze the optical and electronic properties of monolayer MoS_2 and evaluate its suitability for optoelectronic and gas-sensing applications. By systematically tuning the interlayer separation, we investigate how the formation of a MoS_2/graphene heterostructure can induce a finite band gap in graphene, thereby enhancing its sensitivity toward hazardous gases such as CO, CO_2, HF, and NO. In particular, we examine the influence of interlayer coupling on the band structure, density of states, and optical absorption, and correlate these modifications with the adsorption energetics at the heterointerface. This integrated approach provides a comprehensive framework for designing MoS_2/graphene heterostructures as high-performance, multifunctional platforms for advanced optoelectronics and next-generation gas-sensing technologies.

2. Methodology

DFT calculations were performed using the Quantum ESPRESSO suite, employing the plane-wave pseudopotential framework to probe the structural stability and optical

response of the MoS_2/graphene heterostructure. Exchange-correlation effects were treated using the Perdew–Burke–Ernzerhof (PBE) functional within the generalized gradient approximation (GGA) [61], and long-range dispersion interactions were explicitly accounted for through the Grimme van der Waals (vdW) correction [62], which is essential for accurately describing interlayer coupling in van der Waals heterostructures. Self-consistent field (SCF) calculations were converged to 10^{-4} eV, and for monolayer MoS_2, atomic geometries were optimized until the residual forces were below 0.01 eV·Å^{-1} for monolayer MoS_2. The Brillouin zone was sampled along the Γ-M-K-Γ path using a 6 × 6 × 1 Monkhorst–Pack mesh, with a 2 × 2 × 1 supercell and kinetic energy cutoffs of 60 Ry for the wavefunctions and 600 Ry for the charge density. For graphene, wavefunction and charge-density cutoffs of 50 and 460 Ry, respectively, were applied, and structural relaxation was performed until the forces fell below 0.02 eV·Å^{-1}. The graphene band structure was computed using a dense 150 × 150 × 1 k-point grid along the high-symmetry path, ensuring accurate resolution of its Dirac-cone dispersion. For the MoS_2/graphene interface, a more stringent relaxation criterion was adopted (10^{-3} eV·Å^{-1} for forces and 10^{-5} eV for the SCF energy). The heterostructure was constructed by combining a $\sqrt{7} \times \sqrt{7} \times 1$ graphene supercell with a 2 × 2 × 1 MoS_2 supercell, yielding a 26-atom cell comprising 14 C, 4 Mo, and 8 S atoms. The initial in-plane lattice mismatch, evaluated relative to the MoS_2 supercell before a common periodic cell was imposed, was approximately 2.25%. After matching, both layers shared common in-plane lattice parameters of a = b = 6.4351 Å, and $\gamma = 120°$. A vacuum spacing of 15 Å was introduced along the out-of-plane direction to eliminate spurious interlayer interactions. The interlayer distance d, defined as the vertical separation between the carbon plane and the nearest sulfur plane, was imposed between 2.3 and 3.2 Å by fixing the out-of-plane atomic coordinates. Calculations at 2.1 and 2.0 Å were also attempted but did not reach SCF convergence and were therefore excluded. The adsorption energies of CO, CO_2, NO, and HF molecules on the MoS_2/graphene surface were subsequently evaluated using the same PBE-GGA framework. Each gas/heterostructure configuration was optimized within a 15 Å vacuum region to avoid periodic image effects, and the initial vertical separation between the molecule and the surface was set at 2.5 Å to ensure a consistent and unbiased starting geometry. Collectively, this computational approach provides a robust and high-fidelity description of the MoS_2/graphene interface and its molecular adsorption behavior, establishing a solid foundation for assessing its potential in next-generation sensing and optoelectronic applications.

3. Results and Discussion

3.1. Properties of MoS_2

Monolayer MoS_2 adopts a hexagonal lattice in which each Mo atomic plane is covalently bonded to two S planes, forming an S-Mo-S sandwich, as illustrated in Figure 1a–c. The electronic band structure and the corresponding total density of states (DOS) shown in Figure 1d reveal a direct band gap of 1.72 eV at the K point, in close agreement with the experimental value of 1.80 eV [63]. This direct band gap implied that optical transitions from the valence band (VB) to the conduction band (CB) occur without a change in crystal momentum, a hallmark of efficient light-matter interaction in 2D semiconductors. The emergence of this direct band gap is intrinsically linked to the absence of interlayer coupling, as the system consists of a single, electronically isolated MoS_2 sheet.

The structural parameters of MoS_2 were determined using the PBE-GGA functional and are summarized in Table 1. The calculated values show excellent agreement with experimental measurements. providing a robust foundation for subsequent electronic and optical property analyses.

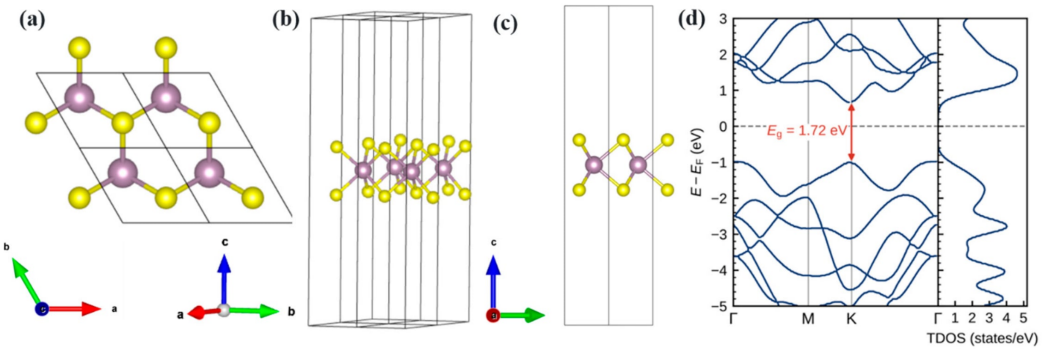


Figure 1. Lattice structure and electronic properties of monolayer MoS_2: (**a**) top view; (**b**) three-dimensional view; (**c**) side view of the relaxed hexagonal S-Mo-S lattice (yellow spheres: S atoms; purple spheres: Mo atoms); (**d**) calculated total DOS and electronic band structure along the high-symmetry path Γ-M-K-Γ, showing a direct band gap of ~1.72 eV at the K point.

Table 1. Comparison of lattice parameters of MoS_2 monolayer between different approaches and the experiment.

a ($A°$)	c ($A°$)	Exchange-Correlation Functional	Reference
3.16	No layers in the z axis	GGA using PBE	This work
3.11		Local density approximation (LDA)	[64]
3.23		GGA using PBE	[65]
3.16		Experiment	[66]

The optical response of monolayer MoS_2 was investigated over the 350–1000 nm spectral range, with a focus on its complex dielectric function, which fundamentally dictates the material's interaction with electromagnetic radiation. As a central descriptor of light-matter coupling, the dielectric function governs excitonic effects, absorption resonances, and overall optoelectronic performance. The real $\varepsilon_r(\omega)$, and imaginary $\varepsilon_i(\omega)$, components of $\varepsilon(\omega)$ were extracted using the Kramers–Kronig transformation, providing a rigorous and internally consistent framework for quantifying the optical behavior of MoS_2 at the monolayer limit [67]. The complex dielectric function is expressed as:

$$\varepsilon(\omega) = \varepsilon_r(\omega) + i\varepsilon_i(\omega) \quad (1)$$

The real component of the dielectric function, $\varepsilon_r(\omega)$ describes the polarization response of the material under an external electromagnetic field, whereas the imaginary component, $\varepsilon_i(\omega)$, quantifies the dissipative part of the interaction, providing direct insight into the material's light-absorption capability. Several key optical properties, including the refractive index $n(\omega)$, extinction coefficient $k(\omega)$, absorption coefficient $\alpha(\omega)$, and reflectance $R(\omega)$, can be derived directly from these dielectric components. The absorption coefficient $\alpha(\omega)$ specifies the rate at which light intensity decays as it propagates through the material and is directly governed by both $k(\omega)$ and the photon energy. Likewise, the reflectance $R(\omega)$ at the material surface depends on the combined contributions of $n(\omega)$ and $k(\omega)$. All these quantities were evaluated using the following standard relationships [68–70]:

$$n(\omega) = \left(\frac{\left(\left[\varepsilon_r^2(\omega) + \varepsilon_i^2(\omega)\right]^{\frac{1}{2}} + \varepsilon_r(\omega)\right)}{2}\right)^{\frac{1}{2}} \quad (2)$$

$$k(\omega) = \left(\frac{\left(\left[\varepsilon_r^2(\omega) + \varepsilon_i^2(\omega)\right]^{\frac{1}{2}} - \varepsilon_r(\omega)\right)}{2}\right)^{\frac{1}{2}} \quad (3)$$

$$\alpha(\omega) = \frac{2\omega k(\omega)}{c} \quad (4)$$

$$R(\omega) = \frac{(n(\omega)-1)^2 + k^2(\omega)}{(n(\omega)+1)^2 + k^2(\omega)} \quad (5)$$

where c is the speed of light in a vacuum and ω representing the frequency of the incident wave.

The real and imaginary components of the dielectric function of monolayer MoS_2, evaluated along both the in-plane (parallel) and out-of-plane (perpendicular) directions, are presented in Figure 2a,b.

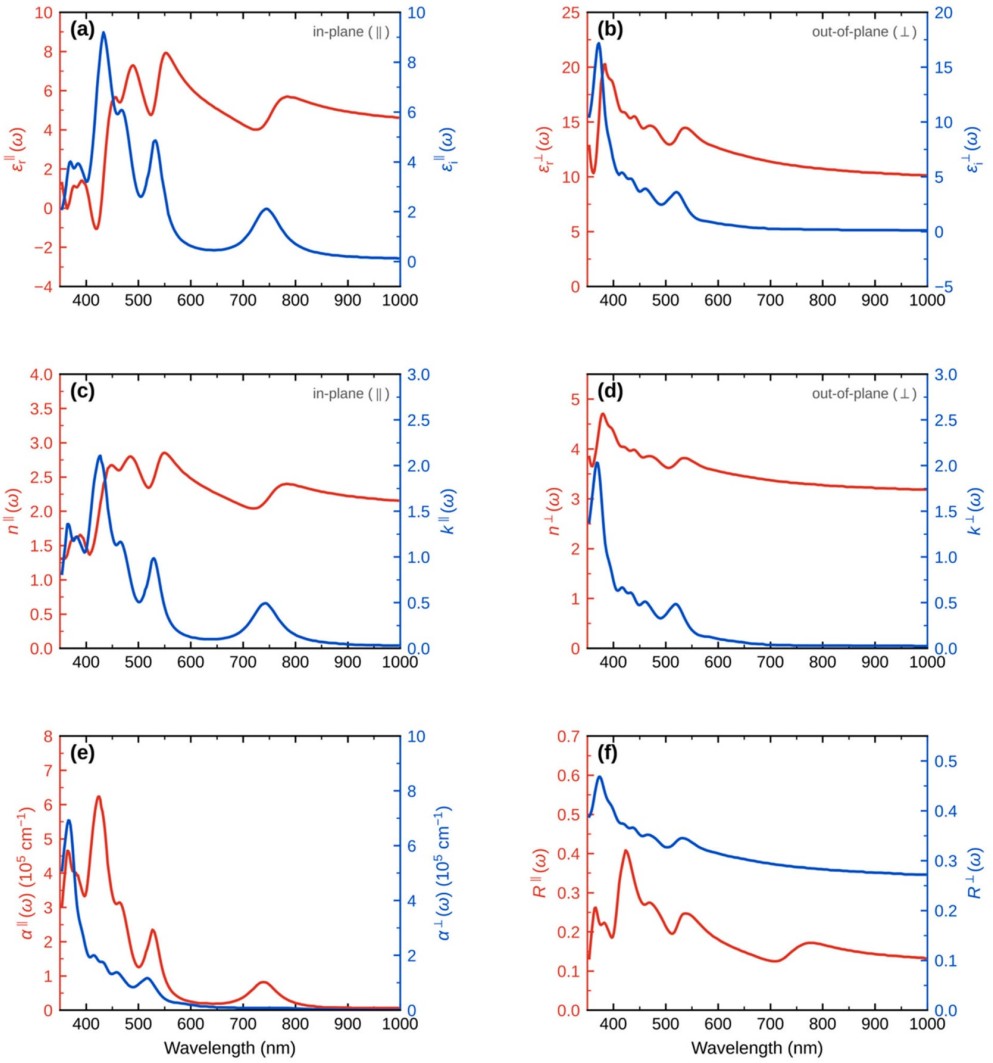


Figure 2. Real and imaginary components of dielectric constant of MoS_2 monolayer: (**a**) along the parallel direction; (**b**) along the vertical direction. Refractive index and extinction coefficient: (**c**) along the parallel direction; (**d**) along the vertical direction. (**e**) Absorption coefficient; (**f**) reflectance along the parallel and the vertical direction.

Along the in-plane direction, $\varepsilon_i(\omega)$ exhibits a pronounced maximum at 425 nm, consistent with previously reported values [71,72], which indicates strong optical absorption at this wavelength. The corresponding $\varepsilon_r(\omega)$ values oscillate between −1 and 8 across the visible region before stabilizing in the infrared, reflecting the dispersive nature of the monolayer's electronic polarization. In the out-of-plane direction, $\varepsilon_i(\omega)$ displays a sharp peak at 380 nm, followed by a secondary maximum near 525 nm, both characteristic of strong optical transitions in the UV–visible range (Figure 2b). Beyond these features, $\varepsilon_i(\omega)$

gradually decreases toward zero in the infrared, confirming that monolayer MoS_2 acts as an efficient absorber in the UV–vis spectral window while exhibiting minimal absorption at longer wavelengths.

Along the parallel (in-plane) direction of monolayer MoS_2, the refractive index $n(\omega)$ exhibits a broad peak in the visible region, reaching a maximum of ~2.7 within the range of 450–550 nm. A secondary peak of ~2.5 appears in the near-IR region around 800 nm (Figure 2c). These elevated $n(\omega)$ values indicate that light propagates more slowly through the monolayer at these wavelengths, reflecting strong light-matter coupling between the incident electromagnetic field and the Mo-S lattice. This behavior is consistent with prior theoretical studies [72]. In the same in-plane direction, the extinction coefficient $k(\omega)$ displays a dominant peak in the visible region with a maximum of ~2.7, followed by a secondary peak near 1.2, before stabilizing at 0.03 in the IR region. Along the vertical (out-of-plane) direction, which corresponds to the monolayer thickness, $n(\omega)$ presents a pronounced peak near 380 nm with a maximum value of ~4.7 (Figure 2d). This feature indicates noticeable attenuation of light propagation through the thickness in the UV–visible range. The corresponding $k(\omega)$ profile also shows a dominant peak around 370 nm, reaching ~2, confirming significant absorption of UV light. Beyond this region, both $n(\omega)$ and $k(\omega)$ decrease markedly toward the visible spectrum and subsequently stabilize in the infrared domain. Figure 2e presents the absorption coefficient $\alpha(\omega)$ along the parallel direction, showing strong absorption in the UV and visible regions. $\alpha(\omega)$ is approximately 2.8×10^5 cm^{-1} at 350 nm and reaches a maximum of about 6.3×10^5 cm^{-1} near 425 nm. Beyond this main peak, absorption generally decreases with increasing wavelength, with weaker features around 530 and 740 nm, before becoming very weak in the IR region [46,73–75]. Figure 2f illustrates the reflectance $R(\omega)$ of monolayer MoS_2 along the parallel direction, showing a broad high-reflectance region in the visible spectrum, indicative of substantial light reflection at these wavelengths. Along the perpendicular direction, strong reflectance is similarly observed in the UV region, in agreement with previous studies [76,77].

3.2. Properties of Graphene

Graphene consists of a single atomic layer of carbon arranged in a 2D hexagonal lattice (Figure 3b), in which each carbon atom forms three σ-bonds with its nearest neighbors, creating the characteristic honeycomb network (Figure 3a). As a first step, the atomic geometry of graphene was optimized so that all subsequent calculations were based on fully relaxed atomic coordinates, thereby minimizing structural defects and enabling accurate prediction of its intrinsic properties. The optimized C-C bond length is 1.42 Å, in excellent agreement with the experimental value [78]. The lattice constant and the cell volume of graphene are a = 2.47 Å and V = 47.44 $Å^3$. According to the DOS and band structure shown in Figure 3c, the CB and VB touch at the K point in the first Brillouin zone, confirming the zero band-gap energy of graphene.

3.3. Properties of MoS_2/Graphene

Graphene's zero-band-gap nature imposes a fundamental limitation on its direct use as a semiconductor in optoelectronic applications. To address this constraint, a van der Waals heterostructure consisting of monolayer MoS_2 and graphene was constructed. By systematically tuning the interlayer spacing, we investigated how interfacial coupling modulates the electronic and optical properties of the hybrid system. Figure 4 presents the side, three-dimensional, and top views of the MoS_2/graphene heterostructure for interlayer distances ranging from 2.30 Å to 3.20 Å. This controlled variation enables a detailed assessment of the influence of interlayer separation on the emergent electronic characteristics of the

combined structure, offering insights into band-engineering strategies for next-generation 2D optoelectronic devices.

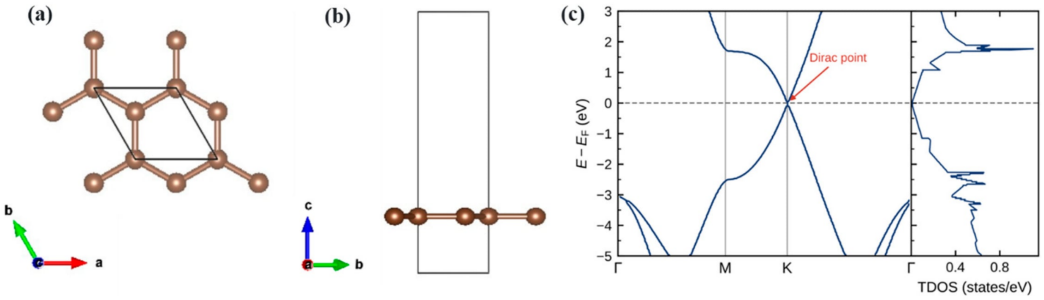


Figure 3. Crystal structure of Gr: (**a**) top view, and (**b**) side view; (**c**) DOS and band structure of Gr.

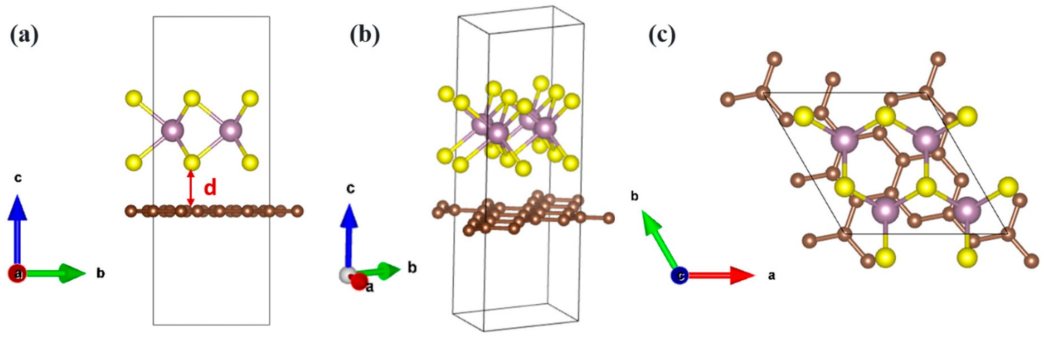


Figure 4. Configuration of MoS_2/graphene heterostructure: (**a**) side view; (**b**) three-dimensional view; and (**c**) top view.

Figure 5a–d present the electronic band structures of the MoS_2/graphene heterostructure for each considered interlayer distance. A clear trend emerges, reducing the separation between the MoS_2 and graphene layers strengthens the interlayer interaction, which in turn induces progressive shifts in both the CB and VB. As highlighted in the magnified views shown in Figure 5e–h, this enhanced coupling results in a gradual opening of the band gap. The appearance of this gap is most plausibly attributed to modifications in the on-site energies of the carbon atoms in the graphene sheet, arising from the perturbation induced by the adjacent of the MoS_2 layer. Such interlayer-coupling-driven band reconfiguration underscores the potential of vdW assembly as an effective strategy for engineering electronic gaps in semi-metallic 2D materials.

The stacking of MoS_2 with graphene enhances interlayer charge transfer, which directly contributes to the opening of a finite band gap in otherwise gapless graphene. Among the converged configurations investigated, the largest band gap, 67.8 meV, was obtained at an interlayer separation of 2.3 Å. In contrast, increasing the spacing to 3.2 Å substantially weakens the electronic coupling, reducing the band gap to 5 meV. This trend is corroborated by the total DOS (TDOS) shown in Figure 6a, as the interlayer distance decreases, a pronounced depletion emerges around the Fermi level. For larger separations, a finite TDOS persists at the Fermi energy, whereas at 2.3 Å the TDOS nearly vanishes, in full agreement with the band-structure analysis, which indicates a widening of the band gap at reduced spacing.

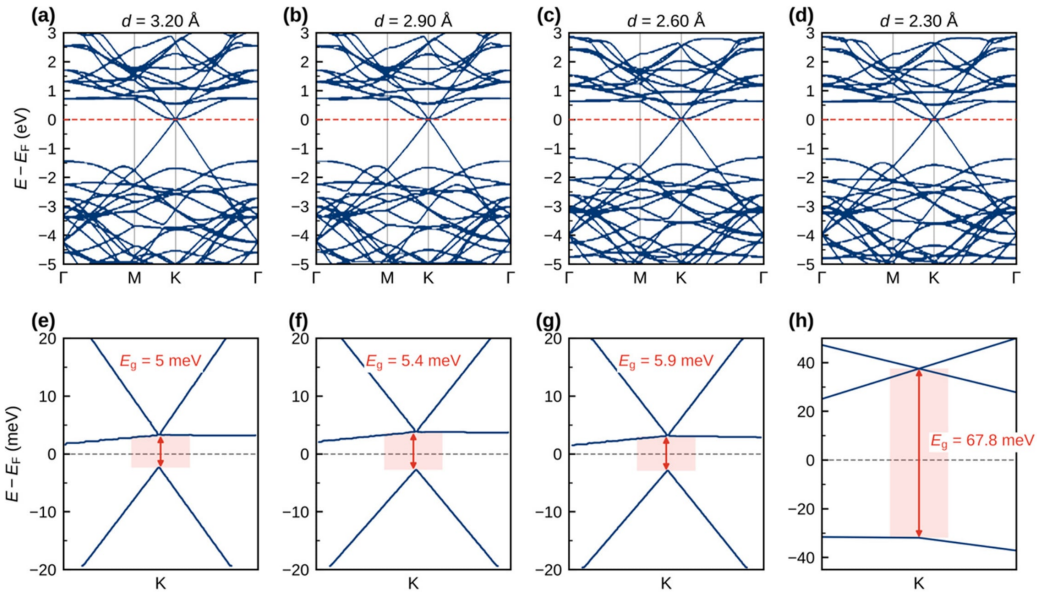


Figure 5. Bands structure of MoS_2/graphene heterostructure at various interlayer distances: (**a**) d = 3.2 Å; (**b**) d = 2.9 Å; (**c**) d = 2.6 Å; (**d**) d = 2.3 Å; (**e**–**h**) shows the zoom in of the band structure near fermi energy of 3.2; 2.9; 2.6; and 2.3 Å, respectively.

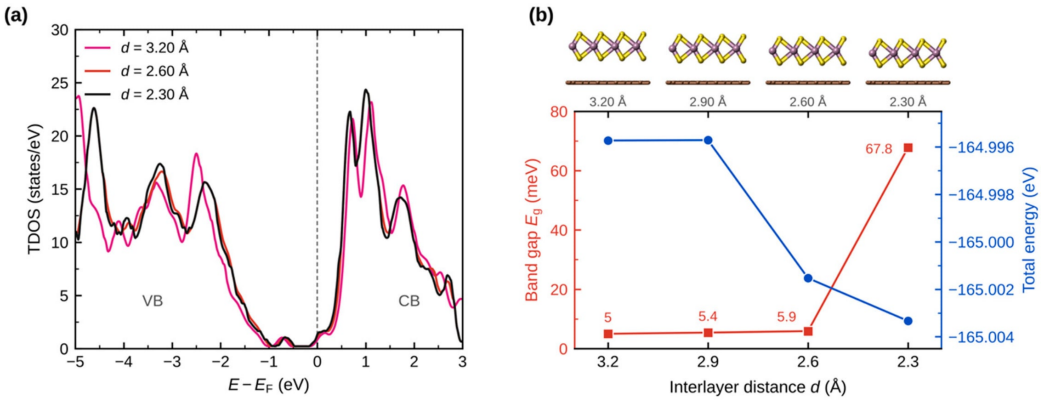


Figure 6. (**a**) Total density of states (DOS) of the MoS_2/graphene heterostructure at various interlayer distances; (**b**) band gap energy (red curve) and total energy of the system (blue curve) as a function of interlayer distance.

Figure 6b further supports this interpretation: the total energy of the heterostructure (blue curve) decreases monotonically with decreasing interlayer distance, reaching its lowest value among the converged configurations investigated at 2.3 Å. Calculations at 2.1 and 2.0 Å were performed alongside the other configurations during the original study but did not converge; consequently, these points were excluded from Figure 6b. Enhanced overlap between the S 3p and out-of-plane C 2p orbitals at these compressed separations may contribute to these convergence difficulties. The simultaneous increase in band-gap energy (red curve) and decrease in total energy indicate that the 2.3 Å configuration exhibits both the lowest calculated energy and the largest band gap within the investigated range. However, because this point lies at the boundary of the sampled range, the present results do not establish an equilibrium interlayer separation. Together, these results underscore the strong dependence of the heterostructure's electronic structure on

interlayer coupling strength, highlighting van der Waals spacing as a powerful tuning parameter for band-gap engineering in MoS_2/graphene systems.

In the following analysis, we focus on the MoS_2/graphene heterostructure with an interlayer spacing of 2.3 Å, which is treated as a compressed configuration chosen to probe the effects of enhanced interlayer coupling on the optical properties. The goal is to elucidate how the incorporation of graphene modifies the optical response of MoS_2, particularly through the key descriptors $\varepsilon(\omega)$, $n(\omega)$, $k(\omega)$, and $\alpha(\omega)$. As shown in Figure 7, the real part of the dielectric function, $\varepsilon_r(\omega)$, displays pronounced peaks in the UV range (Figure 7a), indicative of enhanced polarization effects under high-energy photon excitation. The imaginary part, $\varepsilon_i(\omega)$, likewise exhibits strong UV peaks (Figure 7b), confirming substantial light absorption in this spectral region.

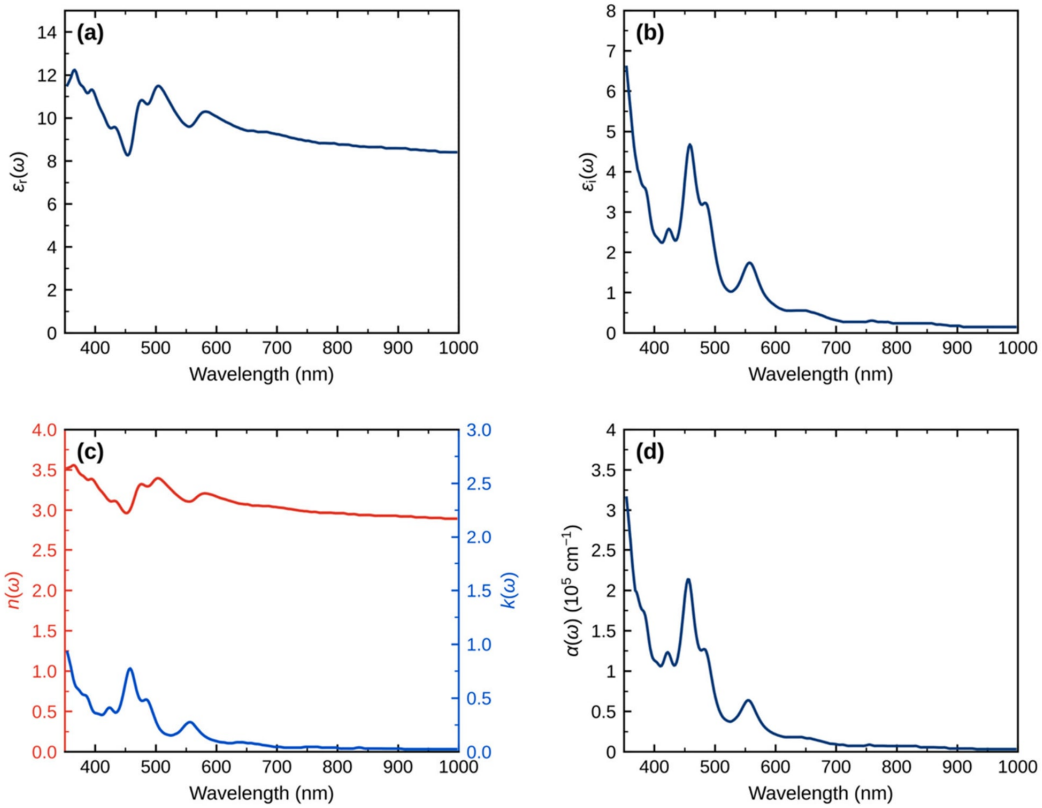


Figure 7. Optical properties of MoS_2/Graphene: (**a**) dielectric function real component; (**b**) dielectric function imaginary component; (**c**) refractive index (red curve) and extinction coefficient (bleu curve); (**d**) absorption coefficient.

Further insight is provided by the refractive index $n(\omega)$ and extinction coefficient $k(\omega)$ (Figure 7c,d). Both quantities attain their highest values in the UV, reflecting intensified light-matter interaction and a corresponding reduction in photon group velocity, characteristic of strong optical confinement. The absorption coefficient $\alpha(\omega)$ also reaches its maximum in the UV region, where high-amplitude absorption peaks with high amplitudes are observed. Beyond this range, $\alpha(\omega)$ decreases sharply across the visible and infrared regions, demonstrating that the optical response of the heterostructure is dominated by UV-driven excitations. At 350 nm in the UV region, the MoS_2/graphene heterostructure exhibits an absorption coefficient approximately 1.2 times that of pristine MoS_2, corresponding to an increase of about 20%. This pronounced improvement highlights the synergistic interplay between MoS_2 and graphene, indicating that interlayer coupling within the heterostructure

can significantly amplify optical activity and broaden its applicability for UV-sensitive optoelectronic technologies.

3.4. Gas Sensing

To investigate the adsorption energies (E_{ads}) of selected gas molecules, namely CO_2, CO, HF, and NO, on the MoS_2/graphene heterostructure, first-principles DFT simulations were performed within the framework of DFT using the PBE-GGA exchange-correlation functional [79]. All calculations were carried out using the Quantum ESPRESSO package [80]. The adsorption energy was computed according to [81]:

$$E_{ads} = E_{MoS_2/Graphene + Gaz} - E_{MoS_2/Graphene} - E_{Gaz} \quad (6)$$

where $E_{MoS_2/Graphene + Gaz}$ is the total energy of the heterostructure with the gas molecule adsorbed, $E_{MoS_2/Graphene}$ is the energy of the pristine heterostructure, and E_{Gaz} is the energy of the isolated gas molecule.

To eliminate spurious interactions between periodic images, a 15 Å vacuum region was introduced perpendicular to the surface to separate periodic images. The initial gas–surface separation was set to 2.5 Å before relaxation. For CO, four initial adsorption sites were investigated (Figure 8b): on top of the Mo atom (A), at the Mo-S bridge site (B), on top of the S atom (C), and at the hollow site at the center of the MoS_2 unit cell (D). Site B gave the lowest adsorption energy for CO among the four sites. For CO_2, HF, and NO, site B was used as a common starting configuration, followed by structural relaxation.

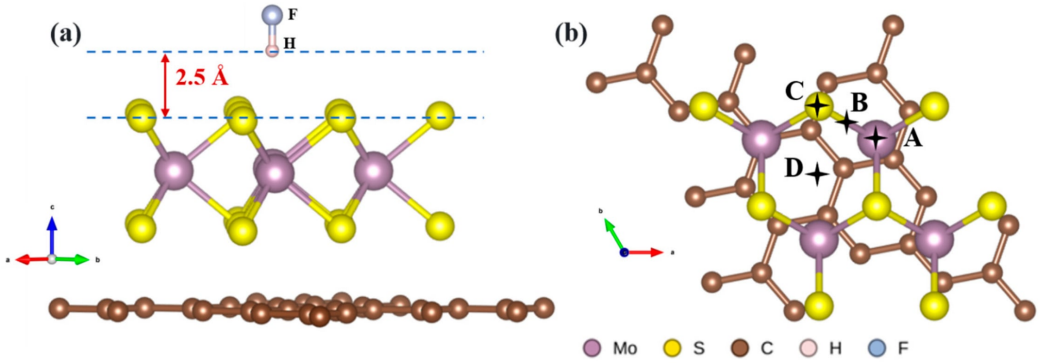


Figure 8. Configurations used for gas sensing evaluation: (**a**) MoS_2/Graphene heterostructure used as the basis of the gas sensor; (**b**) interaction of gas molecules with MoS_2/Graphene placed at various positions: (A) above the Mo atom, (B) between the S and Mo atoms, (C) above the S atom and (D) at the center of the MoS_2 unit cell.

Using DFT simulations, we investigate the complex gas-detection behavior of our nanostructures toward gas molecules such as CO, CO_2, NO, and HF. We aim to uncover subtle structural changes induced by optimization processes and assess their influence on the gas adsorption energies. Table 2 shows the optimized crystalline structures of MoS_2 obtained during the adsorption study of CO gas on four distinct sites (A, B, C, and D). For CO_2, NO, and HF gases, site B was used as the common starting configuration for structural relaxation. These results are compared with our previous work on MoS_2 alone [31].

Table 2 summarizes three key parameters for each gas molecule, the intrinsic bond length of the adsorbate, the equilibrium distance between the molecule and the MoS_2/graphene surface, and the corresponding adsorption energy (E_{ads}). For CO, the adsorption energies range from −70 to −62 meV, with site B giving the most negative value (−70 meV) among the four sites examined. Using site B as the common starting configuration, the calculated adsorption energies for CO_2, HF, and NO are −51, −127, and

−363 meV, respectively. Among the configurations examined, NO shows the strongest binding to the heterostructure, confirming its exceptional sensitivity to the MoS_2/graphene surface toward NO. A comparison with the adsorption behavior on the individual materials reveals that the effect of heterostructure formation depends on the nature of the adsorbed gas. On pristine graphene, CO exhibits only weak physisorption (≈−10.2 meV), and on MoS_2 the interaction is even weaker (≈−5 meV) at site B. In contrast, adsorption on the MoS_2/graphene heterostructure is dramatically strengthened, reaching −70 meV at the same site. A similar enhancement is observed for HF, for which graphene alone yields adsorption energies of about −100 meV, compared with −127 meV on the heterostructure. For NO, the improvement is even more pronounced, where the adsorption on graphene is limited to approximately −29 meV, whereas the heterostructure achieves a much larger interaction energy of −363 meV. For CO_2, adsorption is stronger on pristine graphene (−250 meV) than on the heterostructure (−51 meV).

Table 2. Structural comparison after adsorption of different gas molecule CO, CO_2, NO, and HF at the surface of the MoS_2/Graphene.

Gas	Site	d(Free) (Å) [a]	d(ads) (Å) [b]	h (Å) [c]	E_{ads} MoS_2/Graphene (meV)	E_{ads} MoS_2 (meV)	E_{ads} Graphene (meV)	Q (e) [d]
CO	A	1.144	1.141	3.821	−67	−3.21 [31]	−10.2 [82] [e]	–
	B	**1.144**	**1.141**	**3.652**	**−70**	**−5.03** [31]	–	**0.005**
	C	1.144	1.141	4.297	−62	+0.33 [31]	–	–
	D	1.144	1.141	3.923	−65	−2.41 [31]	–	–
CO_2	B	1.1747	1.1718	3.685	**−51**	−0.66 [31]	−250 [83]	0.005
NO	B	1.1795	1.1707	3.609	**−363**	−260 [84]	−29 [85]	0.057
HF	B	0.95	0.94572	2.262	**−127**	–	−100 [86]	0.036

[a] Bond length of the isolated molecule (C–O, N–O or H–F; for CO_2, the C=O bond). [b] Bond length after adsorption and full relaxation. [c] Final gas–surface distance after relaxation. The initial distance was 2.5 Å in all cases. [d] Bader charge transferred from the heterostructure to the molecule. [e] Value reported for pristine graphene, independent of site.

These results demonstrate that integrating graphene with MoS_2 leverages the high surface area and conductivity of graphene together with the strong binding affinity of MoS_2, producing a synergistic effect that enhances charge transfer and adsorption strength. Consequently, the MoS_2/graphene hybrid exhibits significantly improved gas-sensing performance for three of the four hazardous gases investigated with particularly outstanding sensitivity toward NO, consistent with earlier findings [87].

Moreover, the adsorption process induces subtle structural modifications in the gas molecules, including slight bond-length contractions. Structural relaxation also leads to gas-dependent changes in the gas–surface separation: the distance increases for CO, CO_2, and NO, whereas it decreases for HF. These differences highlight the influence of the nature of the adsorbed molecule on the structural response of the MoS_2/graphene heterostructure and reflect the role of interfacial interactions in modulating adsorption behavior.

To elucidate the electronic origin of these adsorption responses, Bader charge analysis [88] was performed for all four target molecules on the MoS_2/graphene heterostructure (Table 2, Figure 9). The resulting charge-transfer landscape reveals four distinct regimes that correlate directly with both the magnitude of interfacial charge redistribution and the strength of the underlying surface-molecule interaction. For HF, a moderate net charge transfer of approximately 0.036 e from the heterostructure to the molecule is observed, identifying HF as a weak electron acceptor. The accumulated electron density is preferentially localized on the fluorine atom, consistent with its high electronegativity, and the overall

pattern is characteristic of a predominantly physisorptive interaction. In contrast, both CO and CO_2 display essentially negligible charge transfer of approximately 0.005 e, confirming their behavior as very weak electron acceptors whose adsorption is governed almost entirely by van der Waals forces, with CO coupling to the surface even more weakly than HF.

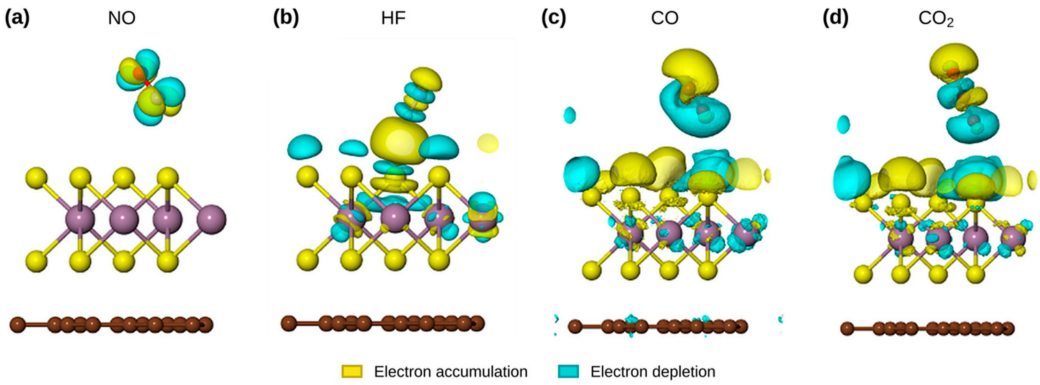


Figure 9. Charge density difference for gas molecules (**a**) NO, (**b**) HF, (**c**) CO and (**d**) CO_2 adsorbed on MoS_2/Graphene heterostructure. Yellow and cyan isosurfaces denote electron accumulation ($\Delta\rho > 0$) and depletion ($\Delta\rho < 0$), respectively. The positive and negative isosurfaces were plotted with magnitudes of (**a**) 2.8×10^{-3}, (**b**) 4.0×10^{-4}, (**c**) 2.0×10^{-5} and (**d**) 3.0×10^{-5} e Bohr^{-3}.

A markedly different regime is observed for NO, which exhibits a substantially higher charge transfer of approximately 0.057 e, identifying it as a strong electron acceptor. The transferred density is concentrated on the nitrogen atom, signaling partial occupation of NO's antibonding π^* orbital and pointing to a more covalent, hybridized interaction with the heterostructure. The NO-MoS_2/graphene system therefore approaches a chemisorption-like regime, a behavior attributable to the radical (open-shell) electronic structure of NO and the resulting orbital availability for charge exchange.

Considered collectively, the Bader analysis establishes a clear hierarchy of interfacial activity, NO $\gg$ HF > $CO_2 \approx$ CO, in which NO emerges as both the most strongly bound and the most electronically perturbing analyte. This hierarchy mirrors the trend observed in the adsorption-energy data discussed above, providing internally consistent computational evidence that the selectivity of MoS_2/graphene heterostructures toward radical, redox-active species is governed not by geometric accessibility alone, but by the orbital-resolved charge-transfer pathways enabled at the heterointerface. This insight is directly relevant to the rational design of selective electronic noses and chemiresistive sensors.

Figure 9 visualizes the charge-density difference (CDD) maps obtained upon adsorption of (a) NO, (b) HF, (c) CO, and (d) CO_2 on the MoS_2/graphene heterostructure, where the yellow and cyan iso-surfaces denote regions of charge accumulation and depletion, respectively. The CDD distributions provide a real-space counterpart to the Bader analysis discussed above and resolve four distinct interfacial coupling regimes. In panel (a), NO induces a pronounced and spatially extended charge redistribution, with strong localization across both the molecule and the underlying MoS_2/graphene region, a hallmark of chemisorption-like coupling driven by the radical (open-shell) electronic structure of NO. In panel (b), HF produces a moderate redistribution that is preferentially concentrated around the fluorine atom, reflecting its role as a weak electron acceptor whose binding remains largely physisorptive. By contrast, panels (c) and (d) reveal that CO and CO_2 generate only faint and diffuse redistribution patterns, consistent with negligible interfacial electron transfer and a purely physisorbed regime. The integrated CDD response therefore follows the hierarchy NO > HF > CO $\approx$ CO_2, in full quantitative agreement with the Bader-

derived charge-transfer trend, and unambiguously identifies NO as the analyte that most strongly perturbs the electronic structure of the MoS_2/graphene heterointerface. To determine whether this preferential coupling is preserved in realistic gas mixtures, additional calculations were performed in which a NO molecule was introduced in the presence of CO_2 as a co-adsorbate. Under these conditions, the adsorption energy of NO is computed to be −294.6 meV, only modestly reduced relative to its isolated value of −363 meV. This limited destabilization (≈19% reduction in binding strength) demonstrates that the presence of CO_2 does not meaningfully disrupt the NO-surface interaction, and that the active sites of MoS_2 within the heterostructure retain their pronounced affinity for NO even in a CO_2-rich atmosphere. This behavior is mechanistically consistent with the substantially stronger interfacial charge transfer for NO (0.057 e), approximately 11 times that for CO_2 (0.005 e), which is approximately 11 times higher. This difference suggests stronger electronic coupling between NO and the MoS_2/graphene heterostructure, whereas CO_2 exhibits weaker charge transfer and less pronounced interfacial interactions. These findings establish that the MoS_2/graphene heterostructure exhibits a high intrinsic selectivity toward NO, robust against CO_2 interference, and they reinforce its potential as a foundational platform for selective, low-cross-talk, room-temperature gas-sensing devices for environmental, industrial, and biomedical monitoring applications.

4. Conclusions

In summary, this work provides a comprehensive first-principles DFT investigation of the structural, electronic, optical, and gas-sensing properties of a MoS_2/graphene van der Waals heterostructure. Our analysis demonstrates that tuning the interlayer spacing serves as an effective strategy for engineering a finite band gap in graphene, with a maximum value of 67.8 meV at a separation of 2.3 Å. This proximity-induced modulation of the electronic structure is further supported by the depletion of the DOS at the Fermi level and the concurrent reduction in total energy. Such control over gap opening is essential for enabling the integration of graphene into semiconducting, optoelectronic, and photonic platforms. The optical analysis reveals that the MoS_2/graphene heterostructure exhibits an absorption coefficient approximately 1.2 times that of pristine MoS_2, corresponding to an increase of about 20% at 350 nm. driven by stronger polarization, increased dielectric response, and intensified light-matter coupling at short wavelengths. This improved optical performance highlights the potential of the heterostructure for UV photodetectors, optical modulators, and energy-harvesting devices. Equally important is the heterostructure's potential for gas-sensing applications, as suggested by the calculated adsorption energies. Among the gases studied (CO, CO_2, NO, HF), NO exhibits the strongest adsorption, reaching −363 meV, which far exceeds the values obtained for pristine graphene or MoS_2. The dramatic enhancement in adsorption energy, e.g., from −29 meV on graphene to −363 meV on the heterostructure, demonstrates a strong synergistic interplay between graphene's high conductivity and MoS_2's strong binding affinity. This synergy leads to improved charge transfer, deeper potential wells, and structurally responsive adsorption geometries. These theoretical findings suggest that the MoS_2/graphene heterostructure is a promising candidate for gas sensing, with preferential NO adsorption among the gases investigated. Experimental validation represents an important direction for future work to assess its sensitivity, selectivity, and performance under realistic operating conditions.

Author Contributions: A.B. (Abderrahim Bayou), A.K., M.A., A.A.-S. and E.M.N. investigation, formal analysis, writing—original draft, A.B. (Abdelkrim Batan) data curation, validation, B.A., B.H. and M.J. conceptualization, validation, supervision. All the authors contributed equally to writing and reviewing the manuscript. All authors have read and agreed to the published version of the manuscript.

Funding: This research received no external funding.

Institutional Review Board Statement: Not applicable.

Informed Consent Statement: Not applicable.

Data Availability Statement: All data of this work are made available from the corresponding author upon request.

Acknowledgments: The authors are grateful to the Region of HDF for financial support.

Conflicts of Interest: The authors declare no conflicts of interest.

References

1. Novoselov, K.S. Nobel Lecture: Graphene: Materials in the Flatland. *Rev. Mod. Phys.* **2011**, *83*, 837–849. [CrossRef]
2. Zhang, S.; Wang, H.; Liu, J.; Bao, C. Measuring the specific surface area of monolayer graphene oxide in water. *Mater. Lett.* **2020**, *261*, 127098. [CrossRef]
3. Zheng, C.; Zhou, X.; Cao, H.; Wang, G.; Liu, Z. Synthesis of porous graphene/activated carbon composite with high packing density and large specific surface area for supercapacitor electrode material. *J. Power Sources* **2014**, *258*, 290–296. [CrossRef]
4. Papageorgiou, D.G.; Kinloch, I.A.; Young, R.J. Mechanical properties of graphene and graphene-based nanocomposites. *Prog. Mater. Sci.* **2017**, *90*, 75–127. [CrossRef]
5. Pang, Y.; Yang, J.; Curtis, T.E.; Luo, S.; Huang, D.; Feng, Z.; Morales-Ferreiro, J.O.; Sapkota, P.; Lei, F.; Zhang, J.; et al. Exfoliated Graphene Leads to Exceptional Mechanical Properties of Polymer Composite Films. *ACS Nano* **2019**, *13*, 1097–1106. [CrossRef] [PubMed]
6. Yang, K.; Wu, C.; Zhang, G. A state of review for graphene-based materials in preparation methods, characterization, and properties. *Mater. Sci. Eng. B* **2024**, *310*, 117698. [CrossRef]
7. Shekhawat, A.; Ritchie, R.O. Toughness and strength of nanocrystalline graphene. *Nat. Commun.* **2016**, *7*, 10546. [CrossRef] [PubMed]
8. Park, W.-Y.; Han, J.; Moon, J.; Joo, S.; Wada, T.; Ichikawa, Y.; Ogawa, K.; Kim, H.S.; Chen, M.; Kato, H. Mechanically Robust Self-Organized Crack-Free Nanocellular Graphene with Outstanding Electrochemical Properties in Sodium Ion Battery. *Adv. Mater.* **2024**, *36*, 2311792. [CrossRef] [PubMed]
9. Lim, M.; Kim, H.-D.; Shim, H.C.; Kim, K.-S.; An, B.-S.; Kim, J.-H. Optically transparent and infrared tunable flexible camouflage device. *Nano Energy* **2024**, *131*, 110189. [CrossRef]
10. Gosling, J.H.; Makarovsky, O.; Wang, F.; Cottam, N.D.; Greenaway, M.T.; Patanè, A.; Wildman, R.D.; Tuck, C.J.; Turyanska, L.; Fromhold, T.M. Universal mobility characteristics of graphene originating from charge scattering by ionised impurities. *Commun. Phys.* **2021**, *4*, 30. [CrossRef]
11. Guo, W.; Zhang, M.; Xue, Z.; Chu, P.K.; Mei, Y.; Tian, Z.; Di, Z. Extremely High Intrinsic Carrier Mobility and Quantum Hall Effect Of Single Crystalline Graphene Grown on Ge(110). *Adv. Mater. Interfaces* **2023**, *10*, 2300482. [CrossRef]
12. Zhou, W.; Ma, T.; Tian, Y.; Jiang, Y.; Yu, X. Dielectric engineered graphene transistors for high-performance near-infrared photodetection. *iScience* **2024**, *27*, 109314. [CrossRef] [PubMed]
13. Kotbi, A.; Lejeune, M.; Oughaddou, H.; Rajput, N.; Zhang, X.; Belhadi, J.; Zakaria, Y.; Richert, D.; Piquemal, F.; Morán-Meza, J.; et al. Eco-Friendly Deposition of Catalyst-Free Graphene on Diverse Substrates. *Adv. Sustain. Syst.* **2025**, *9*, 2500105. [CrossRef]
14. Mouloua, D.; Kotbi, A.; Deokar, G.; Kaja, K.; El Marssi, M.; EL Khakani, M.A.; Jouiad, M. Recent Progress in the Synthesis of MoS_2 Thin Films for Sensing, Photovoltaic and Plasmonic Applications: A Review. *Materials* **2021**, *14*, 3283. [CrossRef] [PubMed]
15. Getaneh, S.A.; Temam, A.G.; Workneh, G.A.; Nwanya, A.C.; Ejikeme, P.M.; Ezema, F.I. Advances in MoS_2-Based ternary nanocomposites for high-performance electrochemical energy storage. *Hybrid Adv.* **2024**, *7*, 100333. [CrossRef]
16. Ouyang, W.; Sofer, R.; Gao, X.; Hermann, J.; Tkatchenko, A.; Kronik, L.; Urbakh, M.; Hod, O. Anisotropic Interlayer Force Field for Transition Metal Dichalcogenides: The Case of Molybdenum Disulfide. *J. Chem. Theory Comput.* **2021**, *17*, 7237–7245. [CrossRef] [PubMed]
17. Raghunathan, M.; Kapoor, A.; Kumar, P.; Laxshmivarahan, A.; Tripathi, S.C.; Ahmad, I.; Pal, D.B. Nanostructured transition metal dichalcogenides-based colorimetric sensors: Synthesis, characterization, and emerging applications. *Luminescence* **2024**, *39*, e4833. [CrossRef] [PubMed]
18. Szary, M.J.; Radomski, P. Unveiling the Chemical Underpinnings behind the Enhanced Adsorption Interaction of NO2 on MoS_2, $MoSe_2$, and $MoTe_2$ Transition Metal Dichalcogenides. *J. Phys. Chem. C* **2023**, *127*, 21374–21386. [CrossRef]
19. Obodo, P.C.; Obodo, K.O.; Aigbe, U.O.; Aigbodion, V. Recent Advances in Molybdenum Disulfide (MoS_2) and MXene-based Heterostructures for Photovoltaic and Water Splitting Applications: A Review. *ChemistrySelect* **2025**, *10*, e202404995. [CrossRef]

20. Coutinho, S.S.; Tavares, M.S.; Barboza, C.A.; Frazão, N.F.; Moreira, E.; Azevedo, D.L. 3R and 2H polytypes of MoS_2: DFT and DFPT calculations of structural, optoelectronic, vibrational and thermodynamic properties. *J. Phys. Chem. Solids* **2017**, *111*, 25–33. [CrossRef]
21. Banu, S.L.; Veerapandy, V.; Fjellvåg, H.; Vajeeston, P. First-Principles Insights into the Relative Stability, Physical Properties, and Chemical Properties of $MoSe_2$. *ACS Omega* **2023**, *8*, 13799–13812. [CrossRef] [PubMed]
22. Gu, M.; Rao, A.M.; Zhou, J.; Lu, B. Molecular modulation strategies for two-dimensional transition metal dichalcogenide-based high-performance electrodes for metal-ion batteries. *Chem. Sci.* **2024**, *15*, 2323–2350. [CrossRef] [PubMed]
23. Thayil, R.; Parne, S.R.; Ramana, C.V. 2D MoS_2 for Next-Generation Electronics and Optoelectronics: From Material Properties to Manufacturing Challenges and Future Prospects. *Small* **2025**, *21*, 2412467. [CrossRef] [PubMed]
24. Jones, L.A.H.; Xing, Z.; Swallow, J.E.N.; Shiel, H.; Featherstone, T.J.; Smiles, M.J.; Fleck, N.; Thakur, P.K.; Lee, T.-L.; Hardwick, L.J.; et al. Band Alignments, Electronic Structure, and Core-Level Spectra of Bulk Molybdenum Dichalcogenides (MoS_2, $MoSe_2$, and $MoTe_2$). *J. Phys. Chem. C* **2022**, *126*, 21022–21033. [CrossRef] [PubMed]
25. Mir, S.H.; Yadav, V.K.; Singh, J.K. Recent Advances in the Carrier Mobility of Two-Dimensional Materials: A Theoretical Perspective. *ACS Omega* **2020**, *5*, 14203–14211. [CrossRef] [PubMed]
26. Schmidt, H.; Wang, S.; Chu, L.; Toh, M.; Kumar, R.; Zhao, W.; Neto, A.H.C.; Martin, J.; Adam, S.; Özyilmaz, B.; et al. Transport Properties of Monolayer MoS_2 Grown by Chemical Vapor Deposition. *Nano Lett.* **2014**, *14*, 1909–1913. [CrossRef] [PubMed]
27. Zhao, X.; Perry, S.S. The Role of Water in Modifying Friction within MoS_2 Sliding Interfaces. *ACS Appl. Mater. Interfaces* **2010**, *2*, 1444–1448. [CrossRef] [PubMed]
28. Kabir, M.H.; Dias, D.; Marjuban, S.M.H.; Avais, M.; Castaneda, H.; Liang, H. Effects of urea-functionalized MoS_2 on hydrophilic lubrication. *Tribol. Int.* **2025**, *203*, 110384. [CrossRef]
29. Tian, X.; Wang, S.; Li, H.; Li, M.; Chen, T.; Xiao, X.; Wang, Y. Recent advances in MoS_2-based nanomaterial sensors for room-temperature gas detection: A review. *Sens. Diagn.* **2023**, *2*, 361–381. [CrossRef]
30. Liu, H.; Zhang, S.; Cheng, Q.; Wang, L.; Wang, S. A Mini Review on the Recent Progress of MoS_2-Based Gas Sensors. *Catal. Lett.* **2024**, *154*, 1375–1384. [CrossRef]
31. Alqaydi, M.; Kotbi, A.; Rajput, N.S.; Bouchalkha, A.; Gagou, Y.; El Marssi, M.; Kasmi, C.; Jouiad, M. Gas sensing capabilities of MoS_2 and WS_2: Theoretical and experimental study. *Emergent Mater.* **2025**, *8*, 5799–5811. [CrossRef]
32. Yan, L.; Shi, H.; Sui, X.; Deng, Z.; Gao, L. MoS_2-DNA and MoS_2 based sensors. *RSC Adv.* **2017**, *7*, 23573–23582. [CrossRef]
33. Nguyen, S.H.; Vu, P.K.T.; Tran, M.T. Absorbance biosensors-based hybrid MoS_2 nanosheets for Escherichia coli detection. *Sci. Rep.* **2023**, *13*, 10235. [CrossRef] [PubMed]
34. Zhao, L.; Wang, Y.; Wei, C.; Huang, X.; Zhang, X.; Wen, G. MoS_2-based anode materials for lithium-ion batteries: Developments and perspectives. *Particuology* **2024**, *87*, 240–270. [CrossRef]
35. Yoo, J.; Zewdie, G.M.; Shin, H. Advancements in MoS_2-based anodes for Li-ion batteries: Recent progress, challenges, and future directions. *Inorg. Chem. Front.* **2025**, *12*, 2587–2612. [CrossRef]
36. Xu, Y.; Wang, Y.; Zhang, C.; Wu, H.; Tan, C.; Hu, G.; Wang, Z. The role of trap states in MoS_2-based photodetectors. *Nanoscale* **2025**, *17*, 9245–9252. [CrossRef] [PubMed]
37. Kwak, D.; Polyushkin, D.K.; Mueller, T. In-sensor computing using a MoS_2 photodetector with programmable spectral responsivity. *Nat. Commun.* **2023**, *14*, 4264. [CrossRef] [PubMed]
38. Bayou, A.; Asbani, B.; Rajput, N.; Mouloua, D.; Campos, A.; Lahmar, A.; Hoummada, K.; Ouaghaddou, H.; Zhang, X.; El Marssi, M.; et al. Unlocking Superior Photodetection Properties of Electrodeposited MoS_2 Quantum Dots. *Small* **2025**, *21*, e08001. [CrossRef] [PubMed]
39. Alfa, I.; Hafeez, H.Y.; Mohammed, J.; Abdu, S.; Suleiman, A.B.; Ndikilar, C.E. A recent progress and advancement on MoS_2-based photocatalysts for efficient solar fuel (hydrogen) generation via photocatalytic water splitting. *Int. J. Hydrog. Energy* **2024**, *71*, 1006–1025. [CrossRef]
40. Das, S.; Acharya, L.; Biswal, L.; Parida, K. Augmented photocatalysis induced by 1T-MoS_2 bridged 2D/2D MgIn2S4@1T/2H-MoS_2 Z-scheme heterojunction: Mechanistic insights into H2O2 and H2 evolution. *Nanoscale Adv.* **2024**, *6*, 934–946. [CrossRef] [PubMed]
41. Bayou, A.; Asbani, B.; Doubi, Y.; Rajput, N.; Campos, A.; El Marssi, M.; Jouiad, M. Superior photoelectrochemical performance of electrodeposited 1T/2H–MoS_2 quantum dots for hydrogen evolution. *Int. J. Hydrog. Energy* **2025**, *139*, 107–115. [CrossRef]
42. Bayou, A.; Asbani, B.; Guilbert, G.; Rajput, N.; Lahem, D.; Jouiad, M. Interface-engineered 1T/2H-MoS_2 on 3D nickel foam enables accelerated hydrogen evolution kinetics. *Int. J. Hydrog. Energy* **2026**, *266*, 157065. [CrossRef]
43. Anushya, G.; Benjamin, M.; Sarika, R.; Pravin, J.C.; Sridevi, R.; Nirmal, D. A review on applications of molybdenum disulfide material: Recent developments. *Micro Nanostructures* **2024**, *186*, 207742. [CrossRef]
44. Im, H.; Kim, J.; Kim, J.; Kim, S. Scalable Bilayer MoS_2-Based Vertically Inverted p–i–n Light-Emitting Diodes. *Adv. Mater. Interfaces* **2024**, *11*, 2300319. [CrossRef]

45. Asbani, B.; Doubi, Y.; Bayou, A.; Rajput, N.; Jouiad, M. MoS_2 quantum dots based next-generation micro-supercapacitors. *J. Energy Storage* **2026**, *153*, 121060. [CrossRef]
46. Tan, F.; Li, J.; Fang, X.; Guan, L. The optical properties of few-layer MoS_2 by DFT calculations. *Physica E Low. Dimens. Syst. Nanostruct.* **2024**, *155*, 115813. [CrossRef]
47. Gusakova, J.; Wang, X.; Shiau, L.L.; Krivosheeva, A.; Shaposhnikov, V.; Borisenko, V.; Gusakov, V.; Tay, B.K. Electronic Properties of Bulk and Monolayer TMDs: Theoretical Study Within DFT Framework (GVJ-2e Method). *Phys. Status Solidi A* **2017**, *214*, 1700218. [CrossRef]
48. Bayou, A.; Asbani, B.; Kotbi, A.; Lejeune, M.; Rajput, N.; Doubi, Y.; Jouiad, M. Mixed-phase electrodeposited MoS_2 quantum dots for solar-driven dye removal. *J. Photochem. Photobiol. A Chem.* **2026**, *474*, 116987. [CrossRef]
49. Conley, H.J.; Wang, B.; Ziegler, J.I.; Haglund, R.F., Jr.; Pantelides, S.T.; Bolotin, K.I. Bandgap Engineering of Strained Monolayer and Bilayer MoS_2. *Nano Lett.* **2013**, *13*, 3626–3630. [CrossRef] [PubMed]
50. Ulian, G.; Valdrè, G. Facile band gap tuning in graphene–brucite heterojunctions. *Sci. Rep.* **2023**, *13*, 23090. [CrossRef] [PubMed]
51. Thomas, N.; Mathew, S.; Nair, K.; O'DOwd, K.; Forouzandeh, P.; Goswami, A.; McGranaghan, G.; Pillai, S. 2D MoS_2: Structure, mechanisms, and photocatalytic applications. *Mater. Today Sustain.* **2021**, *13*, 100073. [CrossRef]
52. Zhang, Y.; Zhao, H.L.; Huang, S.; Hossain, M.A.; van der Zande, A.M. Enhancing Carrier Mobility in Monolayer MoS_2 Transistors with Process-Induced Strain. *ACS Nano* **2024**, *18*, 12377–12385. [CrossRef] [PubMed]
53. Cheng, Z.; He, S.; Han, X.; Zhang, X.; Chen, L.; Duan, S.; Zhang, S.; Xia, M. Improving electron mobility in MoS_2 field-effect transistors by optimizing the interface contact and enhancing the channel conductance through local structural phase transition. *J. Mater. Chem. C* **2024**, *12*, 2794–2802. [CrossRef]
54. Kandhasamy, D.M.; Muthu Mareeswaran, P.; Chellappan, S.; Namasivayam, D.; Aldahish, A.; Chidambaram, K. Synthesis and Photoluminescence Properties of MoS_2/Graphene Heterostructure by Liquid-Phase Exfoliation. *ACS Omega* **2022**, *7*, 629–637. [CrossRef] [PubMed]
55. Chang, K.; Chen, W. L-Cysteine-Assisted Synthesis of Layered MoS_2/Graphene Composites with Excellent Electrochemical Performances for Lithium Ion Batteries. *ACS Nano* **2011**, *5*, 4720–4728. [CrossRef] [PubMed]
56. Li, Y.; Wang, H.; Xie, L.; Liang, Y.; Hong, G.; Dai, H. MoS_2 Nanoparticles Grown on Graphene: An Advanced Catalyst for the Hydrogen Evolution Reaction. *J. Am. Chem. Soc.* **2011**, *133*, 7296–7299. [CrossRef] [PubMed]
57. Vu, S.; Siaj, M.; Izquierdo, R. Graphene-Based Fiber Materials for Gas Sensing Applications: State of the Art Review. *Materials* **2024**, *17*, 5825. [CrossRef] [PubMed]
58. Yoon, H.S.; Joe, H.-E.; Kim, S.J.; Lee, H.S.; Im, S.; Min, B.-K.; Jun, S.C. Layer dependence and gas molecule absorption property in MoS_2 Schottky diode with asymmetric metal contacts. *Sci. Rep.* **2015**, *5*, 10440. [CrossRef] [PubMed]
59. Liu, B.; Chen, Y.; You, C.; Liu, Y.; Kong, X.; Li, J.; Li, S.; Deng, W.; Li, Y.; Yan, H.; et al. High performance photodetector based on graphene/MoS_2/graphene lateral heterostrurcture with Schottky junctions. *J. Alloys Compd.* **2019**, *779*, 140–146. [CrossRef]
60. Zhu, H.; Cheng, Z.; Yuan, Z.; Meng, F.; Zhao, Y. Highly Sensitive EMC Semiconductor Gas Sensor to Overcome Thermal Drift for Thermal Runaway Warning of Lithium Batteries. *IEEE Trans. Instrum. Meas.* **2025**, *74*, 9529109. [CrossRef]
61. Jambrina, P.G.; Aldegunde, J. Chapter 20—Computational Tools for the Study of Biomolecules. In *Tools for Chemical Product Design; Computer-Aided Chemical Engineering*; Martín, M., Eden, M.R., Chemmangattuvalappil, N.G., Eds.; Elsevier: Amsterdam, The Netherlands, 2016; Volume 39, pp. 583–648. [CrossRef]
62. Hua, R.; Diao, C.; Jiang, Y.; Shi, L.; Zhang, C.; Dong, R.Y.; Dong, Y. Effect of van der Waals models on the phonon behavior and thermal conductivity of 2D graphene stacked structure. *Int. J. Heat Mass Transf.* **2025**, *248*, 127202. [CrossRef]
63. Jagosz, J.; Willeke, L.; Gerke, N.; Becher, M.J.M.J.; Plate, P.; Kostka, A.; Rogalla, D.; Ostendorf, A.; Bock, C. Wafer-Scale Demonstration of Polycrystalline MoS_2 Growth on 200 mm Glass and SiO_2/Si Substrates by Plasma-Enhanced Atomic Layer Deposition. *Adv. Mater. Technol.* **2024**, *9*, 2400492. [CrossRef]
64. Nguyen, C.V.; Hieu, N.N.; Nguyen, D.T. Dispersion-Corrected Density Functional Theory Investigations of Structural and Electronic Properties of Bulk MoS_2: Effect of Uniaxial Strain. *Nanoscale Res. Lett.* **2015**, *10*, 433. [CrossRef] [PubMed]
65. Kumar, A.; Ahluwalia, P.K. A first principle Comparative study of electronic and optical properties of 1H—MoS_2 and 2H—MoS_2. *Mater. Chem. Phys.* **2012**, *135*, 755–761. [CrossRef]
66. Wilson, J.A.; Yoffe, A.D. The transition metal dichalcogenides discussion and interpretation of the observed optical, electrical and structural properties. *Adv. Phys.* **1969**, *18*, 193–335. [CrossRef]
67. Gupta, S.; Pimenidou, P.; Garcia, M.; Das, S.; Dimakis, N. Dataset of optical and electronic properties for MoS_2-graphene vertical heterostructures and MoS_2-graphene-Au heterointerfaces. *Data Brief.* **2023**, *49*, 109341. [CrossRef] [PubMed]
68. Makboul, W.; Asbani, B.; Bayou, A.; Rajput, N.; Hartiti, B.; Mounkachi, O.; Jouiad, M. Stabilization of nanoscale ferroelectricity in La-doped HfO2 via defect-engineered phase control: Experimental and theoretical insights. *J. Alloys Compd.* **2026**, *1066*, 188202. [CrossRef]
69. Niu, L.; Conquest, O.J.; Verdi, C.; Stampfl, C. Electronic and Optical Properties of 2D Heterostructure Bilayers of Graphene, Borophene and 2D Boron Carbides from First Principles. *Nanomaterials* **2024**, *14*, 1659. [CrossRef] [PubMed]

70. Prandini, G.; Rignanese, G.M.; Marzari, N. Photorealistic modelling of metals from first principles. *npj Comput. Mater.* **2019**, *5*, 129. [CrossRef]
71. Abbas, A.H.; Mortazavi, S.Z.; Reyhani, A.; Almaamori, M.H.; Khanlary, M.R. Engineering WS_2/MoS_2 thin films via pulsed laser deposition: Structural and optical characterization. *J. Mater. Sci. Mater. Electron.* **2025**, *36*, 1128. [CrossRef]
72. Bouarissa, A.; Gueddim, A.; Bouarissa, N.; Maghraoui-Meherzi, H. Optical response and magnetic moment of MoS_2 material. *Optik* **2020**, *208*, 164080. [CrossRef]
73. Hu, J.-Q.; Shi, X.-H.; Wu, S.-Q.; Ho, K.-M.; Zhu, Z.-Z. Dependence of Electronic and Optical Properties of MoS_2 Multilayers on the Interlayer Coupling and Van Hove Singularity. *Nanoscale Res. Lett.* **2019**, *14*, 288. [CrossRef] [PubMed]
74. Liu, J.; Jin, Y.; Lei, B.; Zhao, X.; Huang, Y.; Zhang, L.; Zhu, Y. Studies on Electronic Structure and Optical Properties of MoS_2/X (X = WSe2, $MoSe_2$, AlN, and ZnO) Heterojunction by First Principles. *Catalysts* **2024**, *14*, 678. [CrossRef]
75. Gerbi, Z.D. Electronic and optical properties of molybdenum disulfide (MoS_2) mono layer using density functional theory (DFT) calculations. *AIP Adv.* **2025**, *15*, 25313. Retraction in *AIP Adv.* **2026**, *16*, 069901. [CrossRef]
76. Kassaye Sibhatu, A.; Teshome, T.; Akin-Ojo, O.; Yimam, A.; Asres, G.A. DFT investigation of the electronic and optical properties of hexagonal MX2/ZrXO (M = W, Mo and X = S, Se) van der Waals heterostructures for photovoltaic solar cell application. *RSC Adv.* **2022**, *12*, 30838–30845. [CrossRef] [PubMed]
77. Lahourpour, F.; Boochani, A.; Parhizgar, S.S.; Elahi, S.M. Structural, electronic and optical properties of graphene-like nano-layers MoX2(X:S,Se,Te): DFT study. *J. Theor. Appl. Phys.* **2019**, *13*, 191–201. [CrossRef]
78. Yang, G.; Li, L.; Lee, W.B.; Ng, M.C. Structure of graphene and its disorders: A review. *Sci. Technol. Adv. Mater.* **2018**, *19*, 613–648. [CrossRef] [PubMed]
79. Perdew, J.P.; Burke, K.; Ernzerhof, M. Generalized gradient approximation made simple. *Phys. Rev. Lett.* **1996**, *77*, 3865–3868. [CrossRef] [PubMed]
80. Carnimeo, I.; Affinito, F.; Baroni, S.; Baseggio, O.; Bellentani, L.; Bertossa, R.; Delugas, P.D.; Ruffino, F.F.; Orlandini, S.; Spiga, F.; et al. Quantum ESPRESSO: One Further Step toward the Exascale. *J. Chem. Theory Comput.* **2023**, *19*, 6992–7006. [CrossRef] [PubMed]
81. Brach, A.; Zaari, H.; Benyoussef, A.; Oubram, O.; Bahmad, L. First-Principles Investigation of a Bilayer g-C3N4/Bilayer h-BN Van der Waals Type-II Heterostructure for Photocatalytic Water Splitting. *J. Phys. Chem. C* **2026**, *130*, 12904–12916. [CrossRef]
82. Wang, W.; Zhang, Y.; Shen, C.; Chai, Y. Adsorption of CO molecules on doped graphene: A first-principles study. *AIP Adv.* **2016**, *6*, 25317.
83. Ehlert, C.; Piras, A.; Gryn'ova, G. CO_2 on Graphene: Benchmarking Computational Approaches to Noncovalent Interactions. *ACS Omega* **2023**, *8*, 35768–35778.
84. Abbas, H.G.; Debela, T.T.; Hussain, S.; Hussain, I. Inorganic molecule (O2, NO) adsorption on nitrogen- and phosphorus-doped MoS_2 monolayer using first principle calculations. *RSC Adv.* **2018**, *8*, 38656–38666. [CrossRef] [PubMed]
85. Gao, H.; Liu, Z. DFT study of NO adsorption on pristine graphene. *RSC Adv.* **2017**, *7*, 13082–13091. [CrossRef]
86. Song, E.H.; Zhu, Y.F.; Jiang, Q. Density functional theory calculations of adsorption of hydrogen fluoride on titanium embedded graphene. *Thin Solid Films* **2013**, *546*, 124–127. [CrossRef]
87. Zhao, S.; Xue, J.; Kang, W. Gas adsorption on MoS_2 monolayer from first-principles calculations. *Chem. Phys. Lett.* **2014**, *595–596*, 35–42. [CrossRef]
88. Tang, W.; Sanville, E.; Henkelman, G. A grid-based Bader analysis algorithm without lattice bias. *J. Phys. Condens. Matter* **2009**, *21*, 084204. [CrossRef] [PubMed]

Disclaimer/Publisher's Note: The statements, opinions and data contained in all publications are solely those of the individual author(s) and contributor(s) and not of MDPI and/or the editor(s). MDPI and/or the editor(s) disclaim responsibility for any injury to people or property resulting from any ideas, methods, instructions or products referred to in the content.